Dynamic Molecular Switches Drive Negative Memristance Mimicking Synaptic Behavior

Yulong Wang,[1†] Qian Zhang,[1†] Hippolyte P.A.G. Astier[1†], Cameron Nickle,[2†] Ziyu Zhang,[1] Andrea Leoncini,[1] Dong-Cheng Qi,[3] Yingmei Han,[1] Enrique del Barco[2], Damien Thompson[4*], and Christian A. Nijhuis[1,5,6*]*

[1]Department of Chemistry, National University of Singapore, 3 Science Drive 3, Singapore 117543, Singapore.

[2]Department of Physics, University of Central Florida, Orlando, Florida 32816 - USA.

[3]School of Chemistry, Physics and Mechanical Engineering, Queensland University of Technology, Brisbane, Queensland 4001, Australia.

[4]Department of Physics, Bernal Institute, University of Limerick, Limerick V94 T9PX, Ireland.

[5]Centre for Advanced 2D Materials and Graphene Research Center, National University of Singapore, 6 Science Drive 2, Singapore 117546, Singapore.

[6]Hybrid Materials for Opto-Electronics Group, Department of Molecules and Materials, MESA+ Institute for Nanotechnology and Center for Brain-Inspired Nano Systems, Faculty of Science and Technology, University of Twente, 7500 AE Enschede, The Netherlands.

[†]These authors contributed equally to this work

*Authors to whom correspondence should be addressed: c.a.nijhuis@utwente.nl, damien.thompson@ul.ie and delbarco@ucf.edu.

One Sentence Summary: A multi-functional molecular switch enables complex dynamic electronic function simplifying brain-inspired electronic devices

Abstract: To realize molecular scale electrical operations beyond the von Neumann bottleneck, new types of multi-functional switches are needed that mimic self-learning or neuromorphic computing by dynamically toggling between multiple operations that depend on their past. Here we report a molecule that switches from high to low conductance states with massive negative memristive behavior that depends on the drive speed and the number of past switching events. This dynamic molecular switch emulates synaptic behavior and Pavlovian learning and can provide all of the fundamental logic gates because of its time-domain and voltage-dependent plasticity. This multi-functional switch represents molecular scale hardware operable in solid-state devices opening a pathway to dynamic complex electrical operations encoded within a single ultra-compact component.

Introduction

Inspired by the energy efficiency of brains and the ever-increasing demand for miniaturized electronics, there is a drive to develop devices that mimic the dynamic character of neurons and synapses to create trainable, adaptive computing networks or new hardware for deep learning for various applications, including pattern recognition, classification, or to realize non-von Neumann neuromorphic computation(*1*–*5*). Neuromorphic computing revolves around emulating synaptic plasticity in electronic systems. Such operations are currently performed using complex, energy-inefficient silicon-based circuits with large footprints, or *mesoscale* memristive systems based on ferroelectric(*6*) or phase change materials(*7*), filaments, or migration of dopants(*1*, *3*, *8*). In this context, molecular switches are appealing because of their inherently small size but molecular switches so far are static, meaning they switch between fixed on and off states (*e.g.*, magnetic, redox, or conformational states)(*9*–*11*). Here we report a dynamic molecular switch in a tunnel junction that remembers its history, whereby the switching probability and the values of the on/off states continually change. This dynamic switch successfully emulates synaptic behavior, Pavlovian learning, and, by exploiting the time-domain plasticity of the junctions, mimics all two-terminal logic gates necessary for deep learning. These functionalities are provided within a single molecular layer (2.4 nm thick), smaller than a neuron synapse (~1-10 μm) by at least three orders of magnitude, and thinner even than the synaptic gap (~20-40 nm) by an order of magnitude. This dynamic nature represents a new class of molecular switch operating far out-of-equilibrium, opening the door to neuromorphic computing at the molecular-scale.

One of the goals of neuromorphic electronics is to produce computing systems where the training is done at the hardware level. So far, molecular hardware for doing

so is not available. Unlike molecular switches studied so far, biological switches, *e.g.*, synapses, are dynamic operating far out of thermodynamic equilibrium(*12*, *13*) and, therefore, can be trained. In synapses (Fig.1**A**), information travels in the form of an action potential from a presynaptic neuron to a postsynaptic neuron through the synaptic gap, as regulated by the combined excitatory and inhibitory neural inputs (*14*). By coupling different processes each characterized with different time constants, *e.g.*, fast depolarization coupled to slow diffusion of Ca^{2+} and neurotransmitters, the synapses can be strengthened or weakened depending on their activity(*15*) resulting in synaptic plasticity enabling pulse pair facilitation and depression with spike rate and timing dependent plasticity. To emulate the dynamical behavior of synapses at the molecular level, we combined fast electron transfer (akin to action potentials and fast depolarization processes) with slow proton coupling limited by diffusion (akin to the role of Ca^{2+} or neurotransmitters).

Solid-state dynamic molecular switches

Fig.1**B-D** shows the dynamic molecular switch (DMS) we introduce here, incorporated in junctions consisting of a self-assembled monolayer (SAM) supported by a gold bottom electrode in contact with an EGaIn top electrode. The SAM molecule has a 5,6,11,12,17,18-hexaazatrinaphthylene (HATNA) terminus that readily undergoes six successive proton coupled electron transfer (PC-ET) steps for dynamic covalent N-H bond formation(*16*, *17*). In the following we indicate the various oxidation states as H_n-HATNA with n=0−6. When the molecules are oxidized (n=0−2) and turn on, electron transfer (ET) across the junctions is fast (fast channel, indicated by a blue arrow) resulting in a large increase of the currents flowing across the junction. In parallel to this fast ET process, proton addition steps occur and N-H

formation slows down the ET rate (slow channel, dashed red arrow) and turns the junction off when HATNA is progressively reduced (n=3−6). In our experiments, water from the ambient (air, room temperature) is the proton source and so proton transfer is diffusion-limited and much slower in nature than ET. This switching from the fast to slow channel occurs at negative bias when the molecules are reduced resulting in a decrease of current and negative differential resistance (NDR). The junctions are oxidized back to their original states by applying a positive bias. Since the ET and proton coupling (PC) steps occur at very different time scales, our junctions can emulate the plastic behavior of synapses, Pavlovian learning, and all logic gates, simply by changing the applied voltage and the duration of voltage pulses.

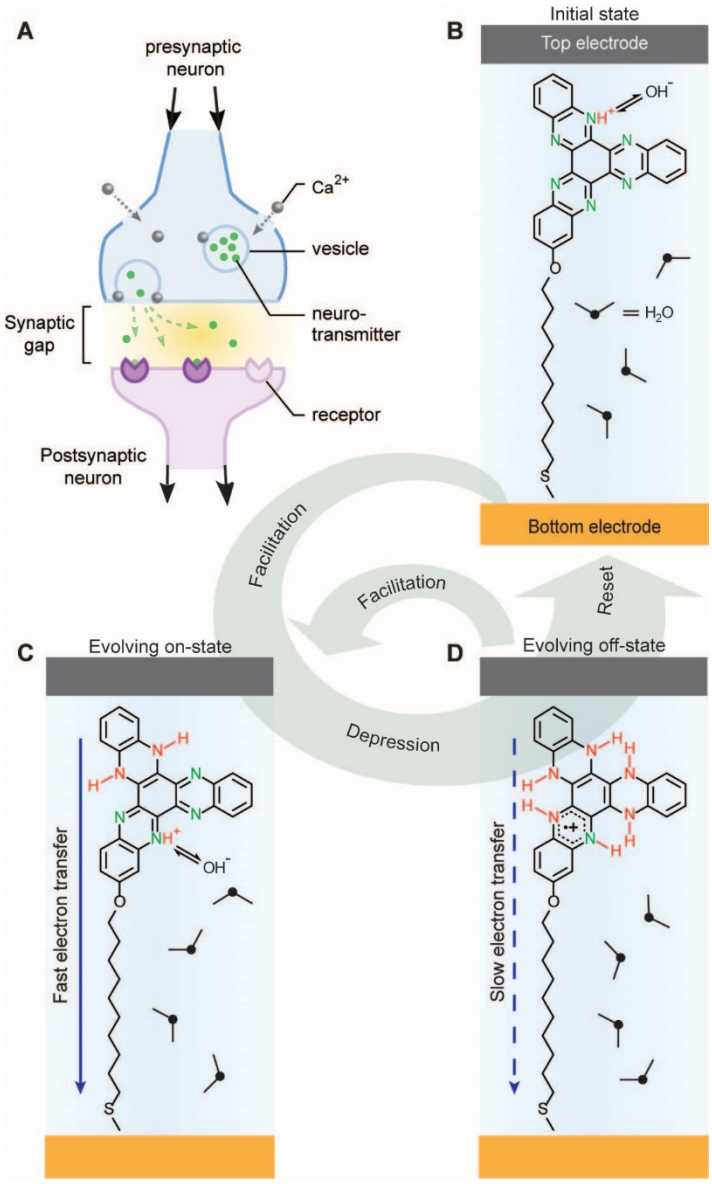

Fig.1. The dynamic molecular junction. (A) Schematic of a synapse and the junctions **(B-D)**. The junction consists of a Au bottom electrode and EGaIn top electrode (EGaIn = eutectic alloy of gallium and indium). Solid and dashed blue arrows indicate electron transfer (ET) *via* coherent tunneling through the fast and slow channels. The two ET channels are bridged by slow proton coupled electron transfer (PC-ET) where the protons are provided by water molecules in air.

Proton-coupled charge transport and dynamic covalent bond formation

We characterized the structure of the SAMs using various techniques (*18*) and conclude that the SAMs are densely packed with all HATNA units confined to the top of the SAM as shown, for instance, by the molecular dynamics simulations (Fig.2**A-C**). To prove that the SAMs undergo sequential PC-ET *via* stable intermediates for reliable switching, we recorded a cyclic voltammogram (CV) from a S-C_{10}-HATNA SAM (Fig.2**D**). Four distinct redox waves are visible which is similar to the results by Ohsaka and co-workers(*17*). They proposed that protonation initiates the first PC-ET step followed by ring-by-ring reduction of HATNA (Fig.2**E**) explaining why the PC-ET cascade appears as distinct redox waves. Our density functional theory (DFT) calculations confirm this mechanism (*18*).

Although the fully reduced SAM has essentially the same supramolecular structure as the SAM in its initial state (Fig.2**C**), our DFT calculations reveal that the electronic structure of the SAM strongly depends on the oxidation and protonation state of HATNA. Fig.2**F** shows projected density of states (PDOS) of the molecule during PC-ET following the steps in Fig.2**G** calculated with DFT. Although the DFT calculations suggest that the HOMO level is close in energy to E_F, the UPS data indicate that the HOMO level is 2.1 eV below the Fermi level of the Au electrode (*18*). Given the common problem of level alignment in DFT calculations(*19*), we rely on the UPS data to properly position the levels with respect to the electrode workfunctions in our energy level diagrams shown in Fig.2**K-P**. Fig.2**G** shows that the molecule in the initial state (H_0-HATNA) has large HOMO-LUMO gap (HOMO=highest occupied molecular orbital, LUMO=lowest unoccupied molecular orbital) of 2.1 eV, but upon initial protonation resulting in (HATNA)H^+, a new midgap state appears around 1.1 eV above the Fermi-energy (E_F) of the Au electrode

providing a low-energy tunneling channel which defines the on-state of the junction (Figs. 1**B** and 2**L-M**). This state persists during the first two PC-ET steps resulting in H_n-HATNA with n=1,2 (Fig.1**C**) but then shifts towards lower energy before disappearing for H_5-HATNA and the large conductance gap is restored (Figs. 1**D** and 2**O-P**), turning the junction off (resulting in NDR as explained below). The changes in HOMO, LUMO, and midgap energy levels during all proton and electron addition steps are given in Fig.2**G** and (*18*).

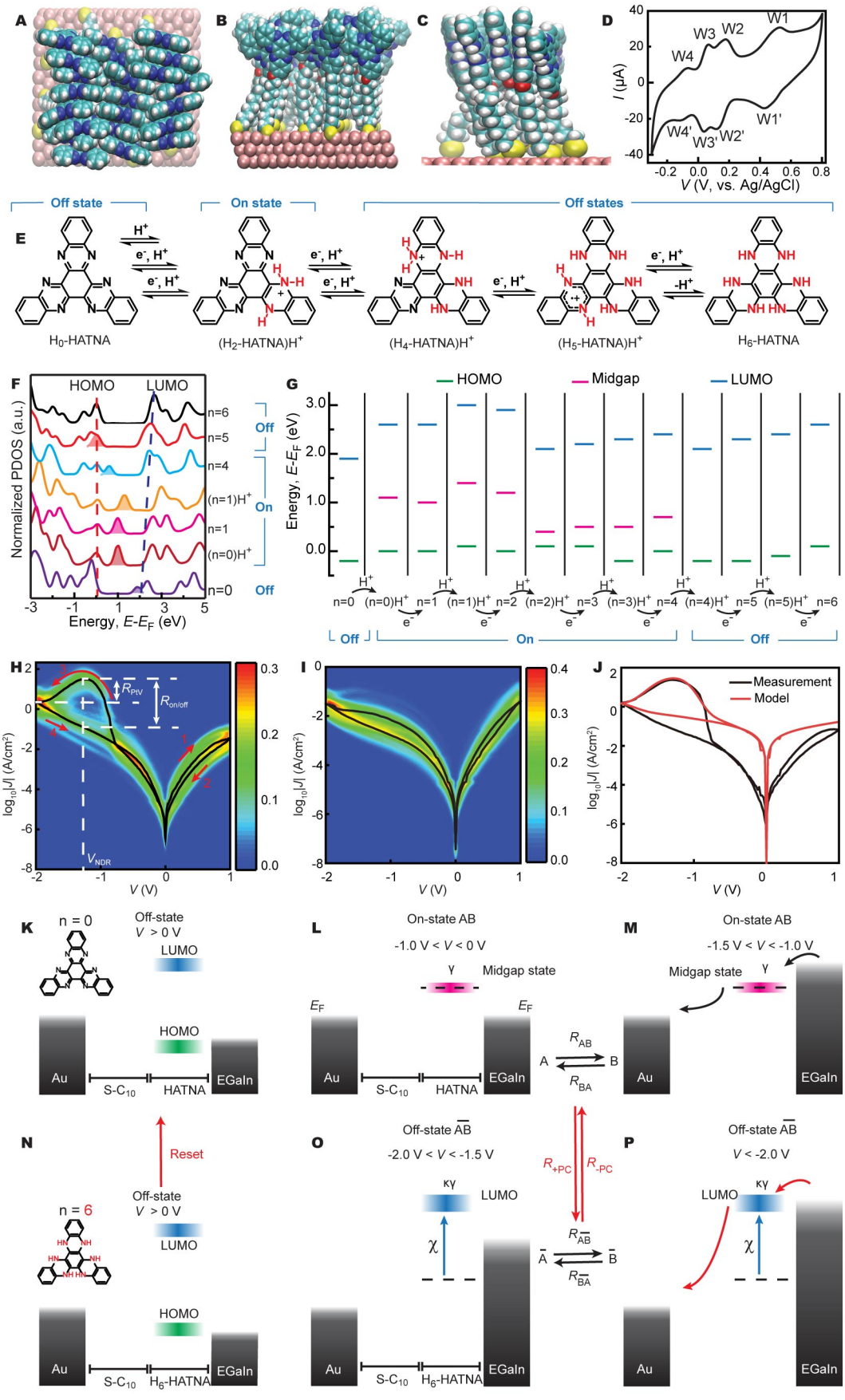
A
B
C
D
W1
W2
W3
W4
W1'
W2'
W3'
W4'
I (μA)
V (V, vs. Ag/AgCl)
Off state
On state
Off states
E
H0-HATNA
(H2-HATNA)H+
(H4-HATNA)H+
(H5-HATNA)H+
H6-HATNA
F
HOMO
LUMO
Normalized PDOS (a.u.)
Energy, E-EF (eV)
n=6
n=5
n=4
(n=1)H+
n=1
(n=0)H+
n=0
Off
On
G
HOMO
Midgap
LUMO
Energy, E-EF (eV)
H
I
J
Measurement
Model
log10|J| (A/cm2)
V (V)
K
n = 0
Off-state
V > 0 V
LUMO
HOMO
Au
S-C10
HATNA
EGaIn
L
On-state AB
-1.0 V < V < 0 V
Midgap state
EF
RAB
RBA
M
On-state AB
-1.5 V < V < -1.0 V
N
Reset
n = 6
H6-HATNA
O
Off-state AB
-2.0 V < V < -1.5 V
R+PC
R-PC
P
Off-state AB
V < -2.0 V

Fig.2. Mechanism of Proton-Coupled Electron Transport. Representative computed structures of π–π driven supramolecular packing in S-C_{10}-HATNA SAMs on Au(111), from 0.1 microseconds of equilibrated room temperature molecular dynamics with H_0-HATNA shown from above (**A**) and from the side (**B**), and a zoom-in on H_6-HATNA shown from the side (**C**). (**D**) Cyclic voltammogram of a HATNA SAM on Au in contact with 2.0 M aqueous $HClO_4$ recorded at scan rate of 0.5 V/s showing four redox-waves labeled W1-4. (**E**) Proposed proton-coupled electron transport (PC-ET) mechanism. (**F**) Calculated projected density of states (PDOS) on the molecule of HATNA SAMs on Au(111) for selected oxidation and protonation states (*18*) and (**G**) the corresponding HOMO, LUMO and midgap energy levels for all states. The oxidation state is indicated by n and the protonation states are indicated by H^+ (*18*). (**H)** Heatmap of $\log_{10}|J|$ *vs. V* (24°C, relative humidity=60% in ambient conditions), and **(I)** Heatmap of $\log_{10}|J|$ *vs. V* measured under an atmosphere of compressed air with 10 ppm water. The black line is log-median average curve ($<\log_{10}|J|>_m$ *vs. V*). (**J**) Shows a representative dataset with a fit to the theoretical model (fitting parameters given in Table S10 of (*18*)).**K-P**, model of the dynamic switch. Energy level diagrams of the off (**K**, **N**-**P**) and on states (**L**, **M**) of the junctions where tunneling is mediated by the acceptor level lying above E_F (blue bar), which is the LUMO at low negative or positive bias (**K-L**) when off resonant tunneling dominates but falls in the conduction window at elevated negative bias when the low-lying midgap state forms because of PC-ET (**M**). The rate equations describe coherent ET tunneling (horizontal transitions) coupled to slow PC steps (vertical transitions). H_6-HATNA can be reset into H_0-HATNA by applying a positive *V* (**N**). PC increases the tunneling barrier height of the ET channel by an interaction energy χ which decreases the molecule–electrode coupling strength γ by a factor κ (resulting in a broad LUMO) (**O**) resulting in NDR. The LUMO in the off state is energetically accessible only at large negative bias (**P**).

Negative differential memristance

Fig.2**H** shows the *J*(V) current density–voltage response from the Au-S-C_{10}-HATNA//Ga_2O_3/EGaIn junctions(*18*). The large hysteric NDR peak can be explained by following the applied voltage in steps 1→4 as indicated. Step1: the voltage increases to +1.0 V which ensures the HATNA moieties are oxidized (n=0). Step2: voltage is reduced and around -0.9 V the current sharply increases as an empty molecular state enters the bias window and the mechanism of charge transport changes from off (Fig.2**K**) to on resonant tunneling (Fig.2**L-M**). The PDOS data indicate that the lowest available tunneling level is the midgap state associated with (HATNA)H^+, which is likely considering the basic nature of HATNA. Step3: with increasing negative bias, the junctions progressively turn on forming H_n-HATNA

with n=1,2 (which have this midgap state), but turn off at large negative bias when molecules are reduced up to H_n-HATNA with n=5,6 (which lack the midgap state) resulting in reduction of current (Fig.2**N-P**) and consequential NDR. Step4: During retrace from -2 to 0 V, junctions remain in the off-state resulting in large hysteretic NDR with a memory (*i.e.*, negative memristance). Only at positive bias, the H_n-HATNA moieties are oxidized to HATNA (n=0) when the HOMO falls inside the conduction window and the cycle restarts (Fig.2**N**). The value of R_{PtV} is 13.7±3.5 (at 10 mV/s) and the value of $R_{on/off}$ is $2.64\pm1.41\times10^2$ which are the among the highest values recorded in molecular junctions(*20*).

Theoretical model for NDR and dynamic switches

There are currently no *ab initio* theories available that can model the dynamical behavior of junctions, but the analytical model developed by Migliore and Nitzan(*21*) captures all our observations as illustrated in Fig.2**K-P** in the form of energy level diagrams which were constructed based on our DFT (Fig.2**F-G**) and spectroscopy results(*18*). The model helps us identify the switching regimes in detail (as demonstrated previously for other switches(*22*)), and more importantly, establishes the mechanism of the time and applied-voltage dependency of the dynamical behavior of the switching. The model describes simultaneous fast ET and slow PC processes in a molecular junction that lead to switching between fast and slow ET channels (Fig.1) as described in detail in (*18*). No molecular orbitals are available for charge transport at low bias (Fig.2**L**) but at intermediate negative bias (step 3, Fig.2**H** and Fig.2**M**) the midgap state enters the conduction window, increasing the ET rates of the on state (R_{AB} and R_{BA} defined in Fig.2**L-M**) after addition of one H^+, *i.e.*, H_0-HATNA→$(H_0\text{-HATNA})H^+$. This protonation step

changes the tunneling barrier height defined by the LUMO to that defined by the midgap state as indicated by χ (Fig.2O-P) and the molecule–electrode coupling strength (given by γ and factor κ). Thus, χ defines the midgap–LUMO energy difference which is 2.1 eV(*18*) in good agreement with DFT (1.5-2.0 eV, Fig.2**G**). At high bias, the HATNA moieties are progressively reduced and junctions turn off again which lowers the ET rates $R_{\overline{AB}}$ and $R_{\overline{BA}}$ (defined in Fig.**2O-P**) resulting in NDR. In parallel, PC (R_{+PC} and R_{-PC}) occurs at much slower rates than ET across both the fast and slow channels (*i.e.*, $R_{+PC} \ll R_{AB},\ R_{\overline{AB}}$), but PC is responsible for switching. Therefore, the ET rates (R_{AB}, R_{BA} and $R_{\overline{AB}}, R_{\overline{BA}}$) and associated currents in the on (I^{AB}) and off ($I^{\overline{AB}}$) state are modelled with a single-level Landauer model(*18*, *23*) while the much slower PC steps (R_{-PC}, R_{+PC}) are described by Marcus theory(*24*) routinely used to model PC-ET steps(*25–27*). Following Migliore and Nitzan's model(*21*), the current that flows across the junctions is calculated from the probability of the junctions to be in the on (P^{AB}) or off ($P^{\overline{AB}}$) state as given by

$$I(V) = P^{AB}(V)I^{AB}(V) + P^{\overline{AB}}(V)I^{\overline{AB}}(V) \qquad (Eqn1)$$

where $P^{AB}(V) = 1 - P^{\overline{AB}}(V)$. The overall dynamical probability of the junction is governed by the slow protonation rates $< R_{+PC} >$ and $< R_{-PC} >$

$$\frac{\mathrm{d}P^{AB}}{\mathrm{d}t} = (1 - P^{AB}) < R_{+PC} > \ - P^{AB} < R_{-PC} > \qquad (Eqn2)$$

Fig.2**J** shows a fit of this model to the *J*(V) data and reproduces all important observations: NDR, hysteretic switching, and the reset at positive bias (which involves the HOMO, Fig.2K,N) (*18*). This modeling of the junction successfully describes the behavior as shown by Figures 2J, 3A and 3G and confirms that the appearance and disappearance of the midgap state causes switching and gives feedback on how and when the protonation occurs by giving an estimate for the

switching probability (Fig.3G). To demonstrate that the presence of water is important, we repeated the experiment with relative humidity <5% where no NDR effect is found (Fig.2**I**).

Emulating synaptic behavior

To demonstrate basic synaptic function with our junctions, we perform pulse-pair facilitation (PPF) and depression (PPD) as follows. Fig.3**A** shows a typical pulse-pair sequence and current response. The difference in chordal conductance ($G=I_{bias}/V$) between the measured and reference pulse in the pair, divided by the chordal conductance of the reference pulse, $\Delta G/G$, is used to quantify PPF and PPD, along with a modelled current response (more examples given in *18*). The magnitude of the voltage pulse (V_p), pulse duration (t_p), and time delay between consecutive pulses (t_d), program the junction. For instance, Fig.3**B** shows that by changing V_p (with $t_p=t_d=1$s) both conductance enhancement (excitatory potentiation) and depression (inhibitory potentiation) are obtained. Fig.3**C** shows that the extent of the potentiation depends on t_p where $\Delta G/G$ follows an exponential decay with characteristic time 2.4 ± 0.9 s(*18*).

Changing the delay between pulses can be used for different programming schemes. No significant decay is found in delays over minutes if the voltage is set at 0 V (*18*). However, the delay voltage can be set to a positive value, *i.e.*, reset voltage V_r, so that the junction will reset over time. Fig.3**D** shows that by changing t_d (with V_p=-2.0 V and t_p=1 s) the conductance decreases exponentially with characteristic time of ~2.5 s (*18*). The speed of this reset process can be adjusted through the magnitude of V_r (Fig.3**E)**. Fig.3**B** shows that spike timing dependent plasticity (STDP), where the order in which the pulses are applied and the delay between them modulates $\Delta G/G$, can also be emulated(*18*). The characteristic decay time of 12 s for positive t_p, and 7s

for negative t_p, are consistent with values obtained from our model (24s and 8s respectively). Spike rate dependent plasticity (SRDP) is shown in Fig.3**F**. A negative inhibitory pulse (V_p = -1.0 V) is applied at a set frequency while a positive excitatory voltage (V_d = 1.25 V) is sustained during the delay between these pulses. Depending on the rate of the inhibitory pulse, the junction can have a net excitatory (46 mHz) or inhibitory (250 mHz) evolution over successive periods. These results demonstrate that, as in biological neural systems(*28*, *29*) the frequency of the signal decides the (synaptic) junction response. This rate control provides a way to create discrete conductance states that can be recognized in subsequent cycles using a number of regular pulses. Fig.3**G** shows that junctions successfully reproduce discretization of ten conductance states; this behavior could be fully modelled. Repeated identical pulses do not potentiate the junction in a constant manner, instead the junctions show habituation, *i.e.*, the junction desensitizes to the signal as the response decays exponentially (as indicated in Fig.3**F**), mimicking how biological systems avoid overstimulation(*30*), This habituation can be reversed through reset pulses and can be explained by the finite number of molecules electrically active in the junction, as captured by the model.

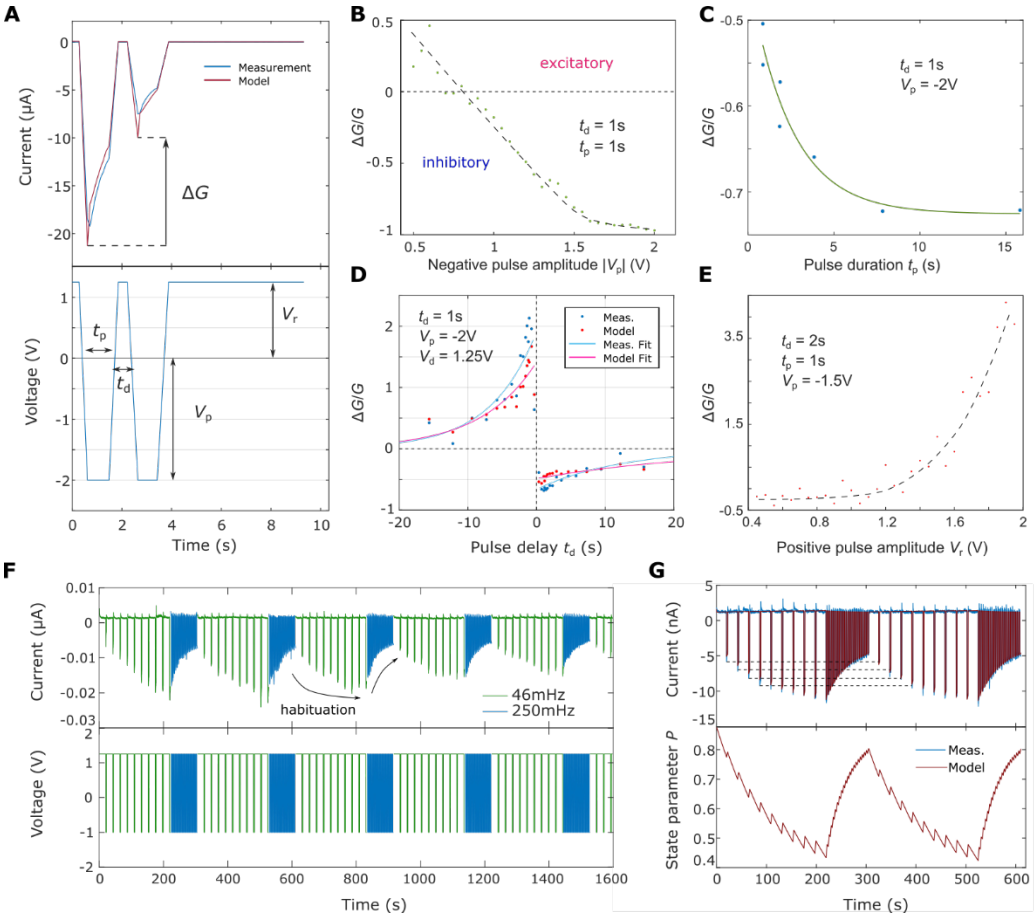

Fig.3. Synaptic function. (**A**) Typical voltage paired-pulse sequence and current response used to extract PPF and PPD properties, as measured (blue line) and fitted by the model (red line) (additional fits are given in *18*)). (**B-E**) $\Delta G/G$ as a function of: (**B**) $-V_p$, (**C**) t_p, and (**D**) t_d with exponential fits (solid lines) used to extract characteristic time constants (*18*), (**E**) V_r, with dashed black lines as a visual guide. The pulse sequences and $I(V)$ profiles of the junctions used are shown in (*18*). (**F**) pulse sequence exhibiting SRDP with V_p=-1V at 46mHz or 250mHz with the inter-pulse delay at V_d=1.25V. The solid black arrows indicate the effects of habituation. (**G**) Identification and retrieval of conductance states over successive cycles and fit to our model. The lower panel shows the evolution of dynamical switching probability P from the model. Dashed black lines are visual guides to show the recovery of the first four conductance states.

Emulating Pavlovian learning and logic gates

The junctions can be incorporated in artificial neural networks (ANNs). Fig.4 shows an ANN that mimics Pavlov's experiment demonstrating the potential for the synapse to serve as a basis for Hebbian learning, *i.e.*, training of an input by simultaneous operation with another input ('neurons that fire together, wire together'(*14*)). Here, two inputs are fired from neurons N1 and N2 (here sources of

voltage pulses) through synapses (electronic junctions) S1 and S2 respectively, to output neuron N3 (an ammeter), as shown in Fig.4**A**. In the Pavlov analogy, N1 represents '*dog sees food*' which readily delivers an output in N3 '*dog salivates*' (Fig.4**B**). The sensitized synapse S1 between the two is materialized by a low-resistance resistor in the circuit. On the other hand, N2 (or '*dog hears bell*') does not readily deliver the output in N3 (see insignificant output in Fig.4**C**, '*dog does not salivate*'), but can be trained to do so through simultaneous operation of N1 and N2 (Fig.4**D**, '*dog sees food and hears bell*'). This sensitizes the adaptive synapse S2, the dynamic switch, and subsequently enables N2 to produce an output in N3 (Fig.4**E**) (*18*). In this set-up, the whole Hebbian learning functionality is provided by the DMS, without the use of a third terminal and additional relays as reported before(*31*).

Components that can perform logic can be used as hidden layers in hardware deep-learning systems(*32*). The time-domain plasticity of the DMS can be used to emulate all standard Boolean logic gates. While the DMS is a two-terminal component and standard logic gates require at least two inputs for one output, the time-domain plasticity of the DMS makes it possible to consider an applied voltage pulse as two separate inputs by separating the voltage and time domains in the pulse. The voltage magnitude of the pulse is one input and its duration a second input, and the resulting modulation in the conductance of the junction represents the output: positive if excitatory, and negative if inhibitory (Fig.4**F-G**). By defining the input states V_{on}, V_{off}, t_{on}, t_{off}, the DMS can provide all of the fundamental logic gates as shown in Fig.4**H-I** (*18*).

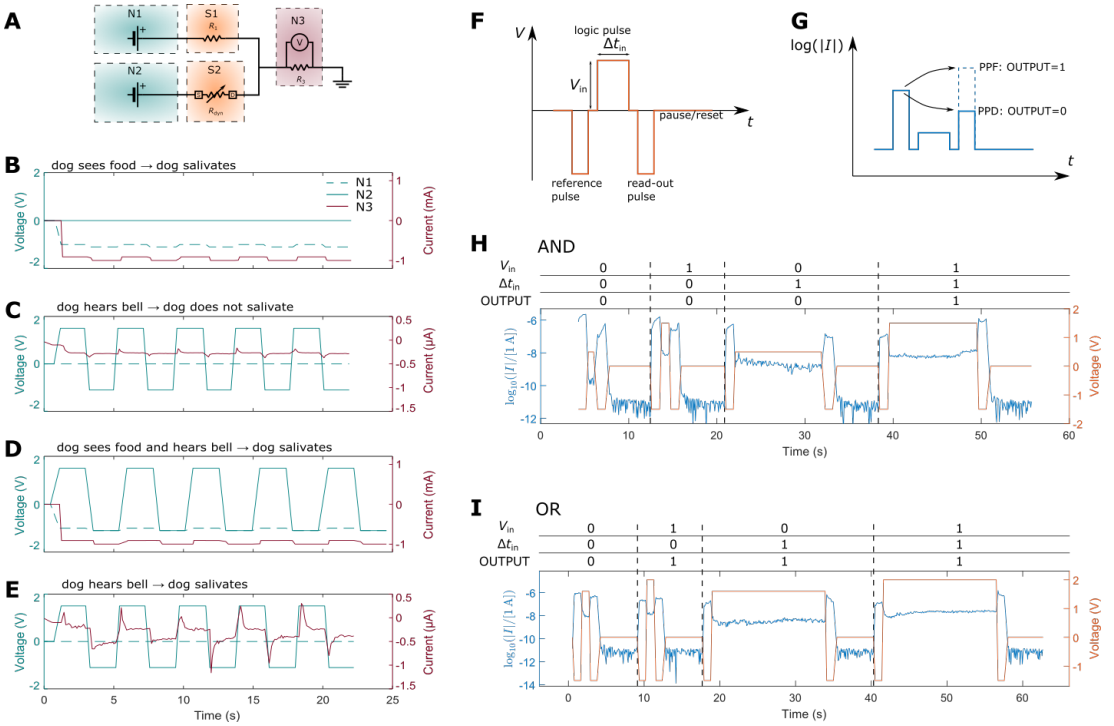

Fig.4. Demonstration of Pavlovian learning and Boolean logic gates using time plasticity in the DMS. (**A**) Schematic of the electrical circuit. Two input neurons N1 and N2 are connected to an output neuron N3 via synapses S1 (resistor) enabling strong coupling between N1 and N3, and S2 (DMS), the trainable synapse. (**B-E**) Pulse sequences showing Pavlovian learning. (**B**) Pulse sequence representing 'dog sees food', pulses from N1 produce a strong output in N3. (**C**) 'dog hears bell' before training, N2 produces an insignificant output in N3. (**D**) 'dog sees food and hears bell', which trains S2. Pulses from N1 and N2 combined produce a strong output in N3. (**E**) 'dog hears bell' after training, N2 now produces a significant output in N3. (**F**) A reference voltage pulse is followed by the logic pulse to perform the operation and finally a read-out pulse. (**G**) The current read-out pulse is compared to the reference pulse, where current increase is defined as output=1 and current decrease as output=0. Demonstration of the AND (**H**) and OR (**I**) logic gates. All other gates and input parameters are shown in (*18*).

Conclusions

We report a dynamic molecular switch of just 2.4 nm that readily emulates the plasticity of synapses, mimics Pavlovian learning, and can be configured to perform all logic gates. Here, the switching probability changes dynamically between high and low conduction states enabled *via* PC-ET driven dynamic N-H bond formation. A challenge is usually to understand the microscopic origin of the dynamics of mesoscale artificial synapses, and such systems are usually modeled with equivalent

circuit analysis or network models. In contrast, the dynamical behavior of our DMS can be readily captured with intertwined rate equations with different time constants and can be applied to dynamic molecular systems driven by other stimuli (such as light(*33*)) and coupled to different types of dynamic covalent bond formation(*34*) opening up a whole new range of adaptive and reconfigurable systems with orthogonal inputs and outputs.

ACKNOWLEDGEMENTS

Funding: We thank the Ministry of Education (MOE, Award No. MOE2018-T2-1-088 and MOE2019-T2-1-137) and the Prime Minister's Office, Singapore, under its Medium Sized Centre program for supporting this research. D.T. acknowledges support from Science Foundation Ireland (SFI) under awards number 15/CDA/3491 and 12/RC/2275_P2 and supercomputing resources at the SFI/Higher Education Authority Irish Center for High-End Computing (ICHEC). E.d.B. and C.N. acknowledge support from the U.S. National Science Foundation (Grant no. ECCS#1916874). D.Q. acknowledges the support of the Australian Research Council (Grant No. FT160100207). **Author contributions:** C.A.N. conceived and supervised the project. D.T. conducted the DFT calculations. E.d.B. and C.N. conducted the numerical modelling. Y.W. synthesized the compounds, Y.W. and Y.H. performed the CV and UV–vis measurements. Z.Z. and D.Q. performed the AR-XPS and NEXAFS measurements and analysis. Y.W. and Q.Z. performed the *I-V* electrical measurements. H.P.A.G.A. designed, performed and analyzed the synaptic emulation measurements. A.L. developed the Origin code for electrical data analysis. C.A.N., E.d.B., D.T., and H.P.A.G.A. wrote the manuscript and all authors commented on it. **Competing interests:** The authors declare no competing interests. **Data and**

materials availability: Data and codes are available in the supplementary materials and at https://dataverse.harvard.edu/privateurl.xhtml?token=efd1a016-cc24-41ab-891b-5217fa6dd56d.

SUPPLEMENTARY MATERIALS

Materials and Methods

Supplementary Text

Figs. S1 to S17

Tables S1 to S10

References 35-66

References

1. Y. Van De Burgt, A. Melianas, S. T. Keene, G. Malliaras, A. Salleo, *Nat. Electron.* **1**, 386–397 (2018).
2. J. Zhu, T. Zhang, Y. Yang, R. Huang, *Appl. Phys. Rev.* **7**, 011312 (2020).
3. N. K. Upadhyay *et al.*, *Adv. Mater. Technol.* **4**, 1800589 (2019).
4. T. Chen *et al.*, *Nature*. **577**, 341–345 (2020).
5. S. T. Keene *et al.*, *Nat. Mater.* **19**, 969–973 (2020).
6. S. Oh, H. Hwang, I. K. Yoo, *APL Mater.* **7**, 91109 (2019).
7. L. Wang, S. R. Lu, J. Wen, Recent Advances on Neuromorphic Systems Using Phase-Change Materials. *Nanoscale Res. Lett.* **12** (2017), pp. 1–22.
8. Q. Wan, M. T. Sharbati, J. R. Erickson, Y. Du, F. Xiong, *Adv. Mater. Technol.* **4**, 1900037 (2019).
9. I. Ratera, J. Veciana, *Chem. Soc. Rev.* **41**, 303–349 (2012).
10. R. Klajn, *Chem. Soc. Rev.* **43**, 148–184 (2014).

11. D. Bléger, S. Hecht, *Angew. Chemie - Int. Ed.* **54**, 11338–11349 (2015).

12. A. Sorrenti, J. Leira-Iglesias, A. J. Markvoort, T. F. A. De Greef, T. M. Hermans, *Chem. Soc. Rev.* **46**, 5476–5490 (2017).

13. S. A. P. Van Rossum, M. Tena-Solsona, J. H. Van Esch, R. Eelkema, J. Boekhoven, *Chem. Soc. Rev.* **46**, 5519–5535 (2017).

14. M. F. Bear, B. W. Connors, M. A. Paradiso, *Neuroscience: Exploring the Brain* (Wolters Kluwer, Philadelphia, 4th Editio., 2016).

15. J. C. Eccles, A. K. McIntyre, *Nature*. **167**, 466–468 (1951).

16. J. L. Segura, R. Juárez, M. Ramos, C. Seoane, *Chem. Soc. Rev.* **44**, 6850–6885 (2015).

17. R. Wang *et al.*, *J. Phys. Chem. B*. **107**, 9452–9458 (2003).

18. Materials, methods, and additional information are available as supplementary materials.

19. D. A. Egger, Z. F. Liu, J. B. Neaton, L. Kronik, *Nano Lett.* **15**, 2448–2455 (2015).

20. M. L. Perrin *et al.*, *Nat. Nanotechnol.* **9**, 830–834 (2014).

21. A. Migliore, A. Nitzan, *J. Am. Chem. Soc.* **135**, 9420–9432 (2013).

22. F. Schwarz *et al.*, *Nat. Nanotechnol.* **11**, 170–176 (2016).

23. A. R. Garrigues *et al.*, *Sci. Rep.* **6**, 26517 (2016).

24. E. D. Fung *et al.*, *Nano Lett.* **19**, 2555–2561 (2019).

25. J. J. Warren, J. M. Mayer, in *Proton-Coupled Electron Transfer: A Carrefour of Chemical Reactivity Traditions* (The Royal Society of Chemistry, 2012; http://dx.doi.org/10.1039/9781849733168-00001), pp. 1–31.

26. A. Migliore, N. F. Polizzi, M. J. Therien, D. N. Beratan, *Chem. Rev.* **114**, 3381–3465 (2014).

27. J. M. Mayer, *Acc. Chem. Res.* **44**, 36–46 (2011).

28. S. Kim *et al.*, *Nano Lett.* **15**, 2203–2211 (2015).

29. Z. Wang *et al.*, *Nat. Mater.* **16**, 101–108 (2017).

30. R. Thompson, in *International Encyclopedia of the Social & Behavioral Sciences* (Pergamon, 2001; https://linkinghub.elsevier.com/retrieve/pii/B0080430767036391), pp. 6458–6462.

31. Y. Van De Burgt *et al.*, *Nat. Mater.* **16**, 414–418 (2017).

32. H. C. Ruiz Euler *et al.*, *Nat. Nanotechnol.* **15**, 992–998 (2020).

33. M. Kathan *et al.*, *Nat. Chem.* **10**, 1031–1036 (2018).

34. P. Chakma, D. Konkolewicz, Dynamic Covalent Bonds in Polymeric Materials. *Angew. Chemie - Int. Ed.* **58** (2019), pp. 9682–9695.